A Dynamic Equivalent of Active Distribution Network: Derivation, Update, Validation and Use Cases

Gilles Chaspierre, *Member, IEEE,* Guillaume Denis, *Member, IEEE,*
Patrick Panciatici, *Fellow Member, IEEE* and Thierry Van Cutsem, *Fellow Member, IEEE*

This paper deals with the derivation of dynamic equivalents of active distribution networks, hosting inverter-based generators as well as static and motor loads. Equivalents are reduced-order models for use in dynamic simulations of the transmission system. They are of the grey-box types and their parameters are identified from large-disturbance Monte-Carlo simulations accounting for model uncertainty. After presenting an overview of the identification method at a single operating point, the paper deals with the update the equivalent when the operating conditions of the distribution network change. A procedure identifies the parameters to update, hence avoiding a complete new identification. Besides illustrative examples, two sets of simulation results are reported. First, the accuracy of the equivalent is validated in a long-term voltage instability scenario. Second, a larger-scale application is presented, with numerous instances of the equivalent attached to the model of the IEEE Nordic transmission test system. This combined model is used to assess the impact on short- and long-term voltage stability of the inverter-based generators with fast and slow controls.

***Index Terms*—active distribution network, inverter-based generator, dynamic equivalent, grey-box model, large-scale dynamic simulations, LASSO method, voltage stability.**

I. INTRODUCTION

ENVIRONMENTAL concerns drive the sustained replacement of conventional generation units, such as Synchronous Generators (SGs), by Inverter-Based Generators (IBGs), mainly PhotoVoltaic (PV) units or Wind Turbines (WTs). For instance, solar energy has become the world's fastest-growing energy technology, with gigawatt-scale markets in an increasing number of countries [1].

Many IBGs are Distributed Energy Resources (DERs) connected to lower voltage levels. Their mere presence already raises new issues in distribution systems. Furthermore, these DERs are more and more requested to provide ancillary services through new types of active and reactive current controls [2]. Hence, the Active Distribution Networks (ADNs) hosting those DERs have a growing influence on the whole power system dynamics. For instance, the replacement of conventional transmission-connected generators by small DERs induces a reduction of the short-circuit level in the transmission grid, which can result in higher voltage sensitivity. It also exacerbates the influence of ADNs on the power system responses to disturbances [3], [4]. Hence, it becomes more and more important for Transmission System Operators (TSOs) to account for the contributions of ADNs in their power system dynamic studies.

A research track followed by some authors is the combined simulation of Transmission and Distribution Systems [5], [6], [7]. However, collecting the whole set of data and matching the operating point of concern is a heavy burden for a TSO. Further, while the Distribution System Operator (DSO) of a Medium-Voltage (MV) and Low-Voltage (LV) grid is usually entitled to collect data about the connected equipment, sharing this information with the TSO comes up against legal issues in some countries.

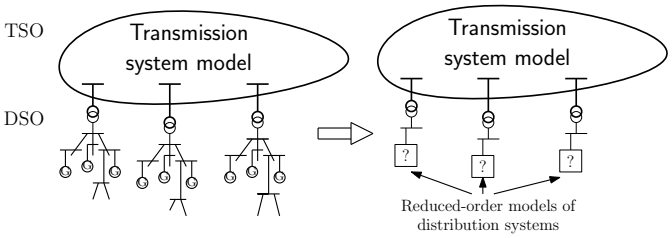

Fig. 1. Replacing ADNs by their equivalents

An appealing alternative consists of DSOs deriving reduced, equivalent models of their own systems. As sketched in Fig. 1, those equivalents are intended to be "attached" to the model of the transmission system for use by the TSO in its power system dynamic studies. The approach is free from confidentiality issues, since the equivalent does not retain the data of individual components.

The approach reported in this paper deals with reduced models of the "grey-box" type [2], [8]. A major advantage of grey-box models is their ability to embed physical knowledge about the original (unreduced) system in the structure of the equivalent, which is appealing from an engineering point of view. Examples of grey-box model identification of ADNs can be found in [9]-[15].

The equivalent is expected to be a good compromise between accuracy and simplicity. Furthermore, the focus is on large disturbances, such as faults in the transmission system. In practice, measurements of the ADN response to such events are little available. This leads to identifying the parameters of the equivalent from time-domain simulations of a representative model of the original system.

This paper is an extension of Ref. [16] and partly builds upon the material presented in [17].

One issue tackled is the update of the equivalent with significant changes of the ADN operating conditions. Although ap-

G. Chaspierre was with the Dept. of Elec. Eng. and Comp. Science, University of Liège, Belgium, e-mail: gilles.chaspierre@kuleuven.be.
G. Denis and P. Panciatici are with the Research & Development Dept., RTE, Paris La Défense, France, e-mail: guillaume.denis@rte-france.com.
T. Van Cutsem was with the Fund for Scientific Research (FNRS) at the University of Liège, Belgium, e-mail: t.vancutsem@uliege.be.

proches such as clustering, probabilistic techniques (e.g. [18]) and artificial neural networks (e.g. [19]) have been proposed to identify and update parameters of black-box equivalents, this aspect has been comparatively little investigated in the context of grey-box models using large-disturbance simulations. It turns out to be impossible for a single set of equivalent parameters to accommodate all possible operating conditions. Instead, the ADN equivalent must be easily updated to accommodate various operating conditions. To that purpose, a method that bears the spirit of the Least Absolute Shrinkage and Selection Operator (LASSO) is proposed. It allows to only update a small subset of the parameters, instead of performing a complete new identification.

The other contributions of the paper are : (ii) to validate the accuracy of the equivalent in a realistic long-term voltage unstable scenario, and (ii) illustrate its use in a large-scale study showing the impact of DERs on short- and long-term voltage (in)stability.

The remaining of the paper is organized as follows. Section II briefly presents the modelling of ADN components. A procedure to derive the ADN equivalent at a single operating point is summarized in Section III, while its update with changing operating conditions is tackled in Section IV. In Section V the accuracy of the equivalent is validated in a long-term voltage instability scenario, while in Section VI a large-scale application is presented combining numerous instances of the equivalent with a transmission system for voltage stability studies. Concluding remarks are offered in Section VII.

II. Modelling of ADN components

The ADN model aims at rendering the impact on transmission system dynamics of the loads and the IBGs dispersed in a distribution grid.

Load and IBG models are outlined hereafter. The models are generic and representative. Note that the methodology is not bound to specific models, and other loads (e.g. [10]) and other IBG controls and types can be accommodated.

Balanced three-phase operation is assumed, as well as dynamic simulations under the phasor approximation [21]. Rotor angle, frequency and voltage stability studies are targeted.

A. Load model

The generic load model is depicted in Fig. 2. It consists of a standard exponential model [21] and a third-order induction motor [21]. P_o (resp. Q_o) is the initial active (resp. reactive) power consumed by the whole load while P_o^{mot} (resp. Q_o^{mot}) is the initial active (resp. reactive) power consumed by the motor part. The reference voltage V_o is set to the initial bus voltage. Initially, the motor consumes a fraction m of P_o and the compensation capacitor is adjusted to satisfy a specified power factor $cos\,\phi_m$.

B. IBG model

The generic IBG model captures the variations of injected current with the terminal voltage. The embedded controls meet recent grid code requirements (e.g. [22], [23]) presented hereafter. The model is described in greater detail in [11].

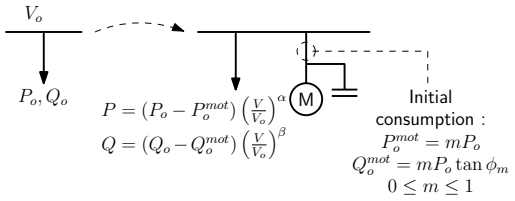

Fig. 2. Load model: decomposition into exponential and motor parts [16]

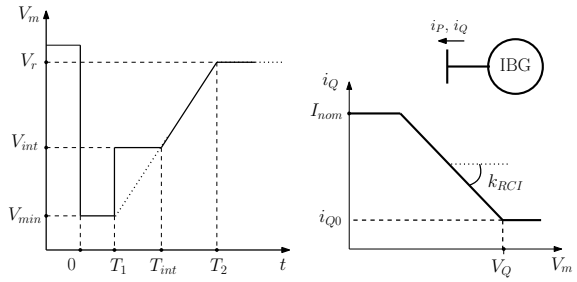

(a) LVRT characteristic (fault occurring at $t = 0$)

(b) Reactive current injection characteristic

Fig. 3. IBG controls responding to large voltage deviations

1) Low Voltage Ride-Through (LVRT)

Grid codes request IBGs above a given rating to remain connected to the grid in low voltage conditions. Yet the units are allowed to disconnect if their terminal voltage falls below an LVRT curve. The curve implemented is defined by six parameters, as shown in Fig. 3.a.

2) Reactive current injection

Grid codes request a large-capacity IBG to inject reactive current into the grid if its terminal voltage falls below some threshold. That current varies linearly with the measured voltage, as shown in Fig. 3.b where i_{Q0} is the initial reactive current, I_{nom} the IBG nominal current and V_m the measured terminal voltage.

3) Current limit

In low voltage conditions, in order to leave room for the reactive current without exceeding the I_{nom} limit, the active current is decreased. For a large enough voltage drop, it may even be forced to zero.

4) Rate of active current recovery

Once the voltage has recovered to normal values, the IBG active current recovers. The recovery cannot be too fast to prevent undesirable fast dynamics. The rate of active current recovery is thus limited to a maximum $(\frac{di_p}{dt})_{max}$.

III. Overview of derivation of an ADN equivalent

This section summarizes the ADN equivalent derivation. The interested reader can find more details in to [16], [17].

A. Dealing with ADN model uncertainty

While grid data are relatively accurate, dynamic models, on the other hand, are affected by uncertainty. This is well known for loads but IBG models are also somewhat uncertain, for instance because grid codes specify typical responses but leave manufacturers with some freedom on the choice of parameters.

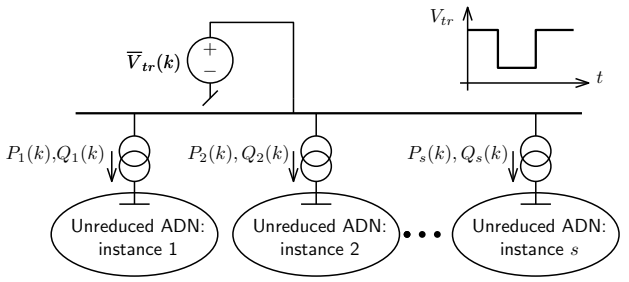

Fig. 4. Disturbance simulation on randomized instances of the ADN model

The impact of these uncertainty can be assessed through Monte-Carlo (MC) simulations. To this end, instances of the ADN model are generated differing by the randomized values of the uncertain parameters. s randomized dynamic responses of a given disturbance are obtained. This is repeated over a set of d "training" disturbances, each of them imposing a large variation of the amplitude, the phase angle, or the frequency of the voltage source $\bar{V}_{tr}$ replacing the transmission system, as shown in Fig. 4.

The variables of interest are the active and reactive powers entering the ADN. Let $P_i(k)$ (resp. $Q_i(k)$) denote the active (resp. reactive) power in the i-th instance of the model $(i = 1, \ldots, s)$, at the discrete time k of the simulation. For the j-th disturbance and the k-th discrete time, the average $\mu_P(j,k)$ (resp. $\mu_Q(j,k)$) and the standard deviation $\sigma_P(j,k)$ (resp. $\sigma_Q(j,k)$) of the $P_i(k)$ (resp. $Q_i(k)$) values are extracted from the MC simulations.

B. Weighted-least square identification of ADN equivalent

Let $\boldsymbol{\theta}$ denote the vector of the ADN equivalent parameters to identify. $\boldsymbol{\theta}$ is adjusted so that, at the various discrete times and for the various disturbances, the active power $P_e(\boldsymbol{\theta}, j, k)$ (resp. reactive power $Q_e(\boldsymbol{\theta}, j, k)$) entering the equivalent approaches in the least square sense the average $\mu_P(j,k)$ (resp. $\mu_Q(j,k)$).

Thus the following constrained optimization is considered:

$$\min_{\boldsymbol{\theta}} \quad F(\boldsymbol{\theta}) = \frac{1}{d}\sum_{j=1}^{d}\left[F_P(\boldsymbol{\theta}, j) + F_Q(\boldsymbol{\theta}, j)\right] \tag{1}$$

$$\text{with} \quad F_P(\boldsymbol{\theta}, j) = \frac{1}{N}\sum_{k=1}^{N}\left[\frac{P_e(\boldsymbol{\theta}, j, k) - \mu_P(j,k)}{\sigma_P(j,k)}\right]^2 \tag{2}$$

$$F_Q(\boldsymbol{\theta}, j) = \frac{1}{N}\sum_{k=1}^{N}\left[\frac{Q_e(\boldsymbol{\theta}, j, k) - \mu_Q(j,k)}{\sigma_Q(j,k)}\right]^2 \tag{3}$$

$$\boldsymbol{\theta}^L \leq \boldsymbol{\theta} \leq \boldsymbol{\theta}^U \tag{4}$$

where N is the number of discrete times of the simulation. The bounds $\boldsymbol{\theta}^L$ and $\boldsymbol{\theta}^U$ keep $\boldsymbol{\theta}$ in realistic ranges of values. Note that each term in (2) (resp. (3)) is weighted by the inverse of the variance $\sigma_P^2(j,k)$ (resp. $\sigma_Q^2(j,k)$) to reflect the dispersion of the MC responses. The termination criterion is:

$$F_P(\boldsymbol{\theta}, j) \leq 1 \quad \text{and} \quad F_Q(\boldsymbol{\theta}, j) \leq 1 \tag{5}$$

meaning that the deviation of $P_e(\boldsymbol{\theta}, j, k)$ from $\mu_P(j,k)$ (resp. $Q_e(\boldsymbol{\theta}, j, k)$ from $\mu_Q(j,k)$) is smaller than $\sigma_P(j,k)$ (resp. $\sigma_Q(j,k)$) on average over discrete times k [16].

A metaheuristic, derivative-free optimization method is used to solve the minimization problem (1)-(4). Among numerous methods, an evolutionary algorithm, namely Differential Evolution (DE) [24] has been chosen, for reasons exposed in [16].

C. Discarding parameters with negligible impact

For computational efficiency as well as consistency and ease of interpretation of the results, the number of components in $\boldsymbol{\theta}$ should be kept minimal, while of course preserving the accuracy of the equivalent [25].

A variant of the LASSO technique has been presented in [16] whose purpose is to identify the components of an initial $\boldsymbol{\theta}$ vector which are "significant". The others have negligible impact and can thus be assigned default values and be removed from $\boldsymbol{\theta}$. The same technique is used in Section IV-B to decrease the burden of updating $\boldsymbol{\theta}$.

D. Training from multiple disturbances

The equivalent is trained from multiple disturbances in order not to overfit one of them. To minimize the computational burden, a procedure has been detailed in [16] to select among an initial set of candidate disturbances those used for training the equivalent, while the others do not bring additional improvement and serve as validation. The principle is to iteratively add to the training set the disturbance with the worst simulated response until the equivalent is found accurate for the rest of the disturbances.

E. Illustrative example of ADN equivalent

The 75-bus 11-kV active distribution test system shown in Fig. 5 is going to be used throughout the rest of the paper. This ADN hosts 22 dispersed IBGs, belonging to two categories:

- large-capacity PV systems for a total capacity of 6.8 MW
- WTs for a total capacity of 8 MW, located closer to the main substation.

All IBGs have LVRT and reactive current injection capabilities. Their total initial production is 9.8 MW. The WTs operate at 80 % of their capacity, and the PV units at 50 %. The loads are connected to the (75-22=) 53 buses with no IBG connected. The total initial consumption is 19.80 MW / 3.40 Mvar. The net power entering the system is 10.33 MW / 3.63 Mvar.

The topology of the grey-box reduced-order model is shown in the right part of Fig. 5. The distribution transformer is preserved, while individual loads (resp. IBGs) are aggregated into a single equivalent load (resp. IBG) connected behind an equivalent impedance $R_a + jX_a$ (resp. $R_b + jX_b$) accounting for network effects. The choice of the equivalent topology is system specific and should reflect the knowledge of the system. For instance, the equivalent IBG and load are connected at different buses to reflect their different locations in the original system, but they could be placed behind the same impedance as in the CMPLDWG model of the Western Electricity Coordinating Council (WECC) [26].

The power entering the equivalent includes the losses in the impedances $R_a + jX_a$ and $R_b + jX_b$, and may not match the power received from the transmission grid via the transformer.

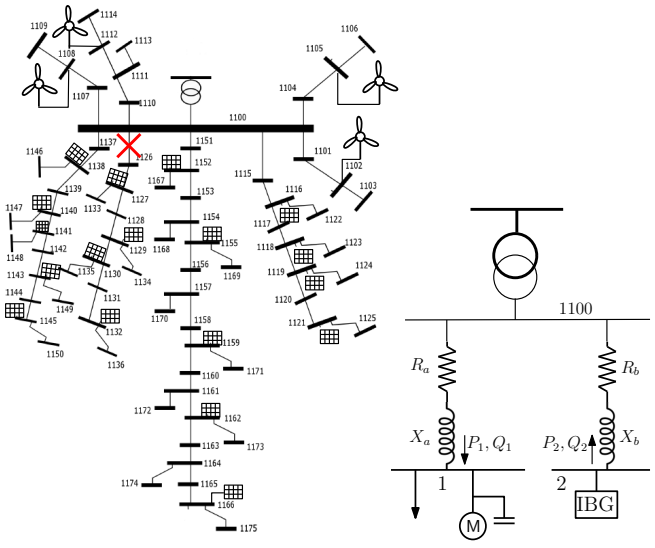

Fig. 5. Unreduced ADN (left) and its grey-box dynamic equivalent (right)

The mismatch is compensated by a "slack load" at the low-voltage bus of the transformer (bus 1100 in the right part of Fig. 5) [16], [17]. This load is treated as constant admittance. Any shunt capacitor connected to the same bus is easily incorporated to the slack load. The effect of shunt capacitors dispersed in the ADN is taken into account when adjusting the exponents of the static part of the equivalent load.

A significant source of uncertainty is linked to the LVRT capability of IBGs. Grid codes usually state that, if its voltage falls and stays below the LVRT curve, an IBG *is allowed but not obliged* to disconnect. Thus, among the IBGs with voltage below the LVRT curve, some disconnect, some do not. This is taken into account by randomizing the disconnection of IBGs (together with other parameters) in the MC simulations. In the equivalent the partial disconnection is accounted for by reducing the power output of the aggregate IBG. More information is provided in [16].

The 13 components of $\boldsymbol{\theta}$ are as follows :

- aggregate static load : α exponent in Fig. 2;
- aggregate motor : rotor resistance, two leakage inductances and loading factor;
- aggregate IBG : nominal current I_{nom}, maximum rate of active current recovery $(\frac{di_p}{dt})_{max}$, slope k_{RCI} and voltage threshold V_Q in Fig. 3.b, three parameters controlling partial disconnection;
- network : X_b reactance.

Other candidate parameters were discarded using the procedure mentioned in Section III-C. Please refer to [16] for more details.

Voltage dips as shown in the upper right corner of Fig. 4 are considered. These disturbances were found most appropriate for training [16]. Fourteen of them are used, corresponding to V_{tr} drops by $10\,k$ $(k = 2, \ldots, 8)$ % during 100 and 250 ms, respectively.

The RAMSES software for dynamic simulation in phasor mode has been used [27]; the average time step size is 0.01 s.

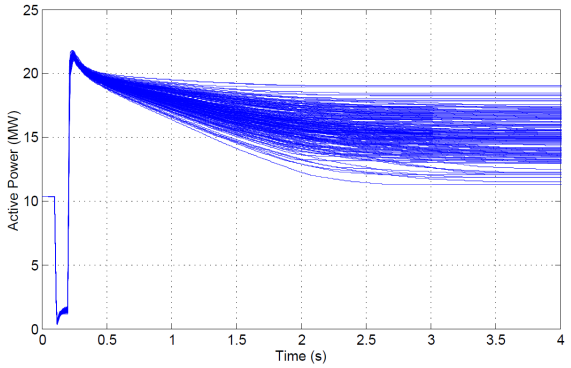

Fig. 6. Randomized evolutions of the active power flowing into the ADN, in response to a voltage dip of 0.8 pu lasting 100 ms (applied at $t = 0.1$ s)

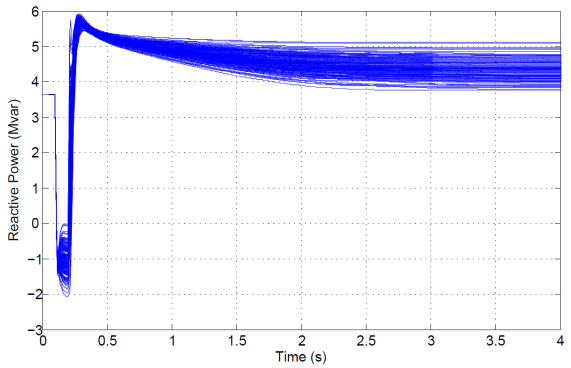

Fig. 7. Randomized evolutions of reactive power flowing into the ADN, in response to a voltage dip of 0.8 pu lasting 100 ms (applied at $t = 0.1$ s)

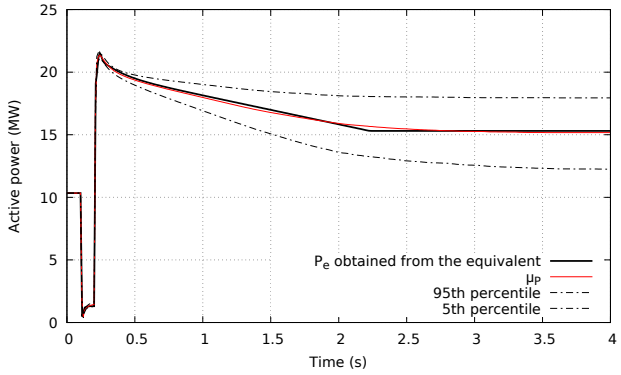

Fig. 8. Active power flowing into the equivalent, compared to the average and the percentiles of the randomized responses shown in Fig. 6

Figures 6 and 7 show the randomized active and reactive power responses of the unreduced system to a severe voltage dip of 0.8 pu lasting 100 ms. The overall evolution is explained as follows. During the voltage dip, the consumption of loads with exponential model decreases while the IBGs sacrifice active current to inject reactive current. This is confirmed by Fig. 7, which shows that the reactive power flow in the main transformer reverses during the voltage dip. When the voltage has recovered its initial value, so do the powers of loads with exponential model, while the motors draw additional power, due to their re-acceleration. The final values testify that some

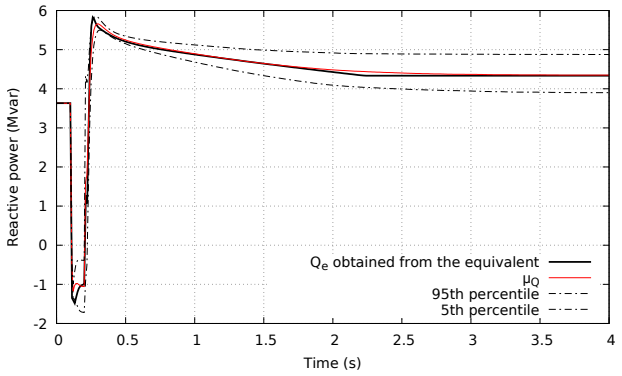

Fig. 9. Reactive power flowing into the equivalent, compared to the average and the percentiles of the randomized responses shown in Fig. 7

IBGs have tripped, the lost generation differing from one randomized response to the other. The still connected IBGs ramp up their active powers back to the initial values.

Figures 8 and 9 show the evolution of the same powers, obtained from the equivalent, for the same disturbance. Note that the latter was not used to train the equivalent. The response of the equivalent matches accurately the average evolution μ_P (resp. μ_Q) extracted from MC simulations, in particular their final values. The 5th and 95th percentile curves recall the dispersion of the responses of the unreduced system and further confirm the accuracy of the equivalent.

The accuracy of the equivalent has been validated on other types of disturbances such as frequency deviations or electromechanical oscillations [16], [17]. An example dealing with long-term voltage instability is detailed in Section V.

Note that no motor stalling has not been observed in the MC simulations of the unreduced sytem nor with its equivalent.

IV. Updating ADN equivalents with operating conditions

ADN equivalents should accommodate a wide range of operating conditions. This is even more relevant since ADNs host renewable and, hence, highly variable generation in addition to the usual varying loads. This motivates the development of a procedure to update the equivalent when it is found not accurate enough under new operating conditions.

A. Overview of the procedure

Assume that a repository of E previously identified equivalents is available, each characterized by a parameter vector $\hat{\boldsymbol{\theta}}$, determined for previous operating conditions. The successive steps for the handling of a new situation are the following.

1) To reflect the change of operating point, the nodal active and reactive powers are updated in the unreduced network;
2) a new operating point requires new MC simulations. For each of the d training disturbance, the statistics $\mu_P^{new}(j)$, $\mu_Q^{new}(j)$, $\sigma_P^{new}(j)$ and $\sigma_Q^{new}(j)$ $(j = 1, ..., d)$ are extracted as explained in Section III-A;
3) the pre-disturbance nodal injections of the equivalent (i.e. P_1, Q_1, P_2, Q_2 in Fig. 5) are obtained by aggregating the nodal active and reactive powers of the unreduced system (see Step 1). The pre-disturbance voltage at the entry point of the ADN (bus 1100 in Fig. 5) is obtained by performing a power flow computation on the unreduced system with the updated nodal powers;
4) the responses of the E equivalents to the d disturbances are simulated, starting from the initial conditions determined at Step 3. From those simulations, the following scores are computed ($i = 1, \ldots, E; j = 1, \ldots d$):

$$F_P^{new}(\hat{\boldsymbol{\theta}}_i, j) = \frac{1}{N}\sum_{k=1}^{N}\left[\frac{P_e(\hat{\boldsymbol{\theta}}_i, j, k) - \mu_P^{new}(j,k)}{\sigma_P^{new}(j,k)}\right]^2 \quad (6)$$

$$F_Q^{new}(\hat{\boldsymbol{\theta}}_i, j) = \frac{1}{N}\sum_{k=1}^{N}\left[\frac{Q_e(\hat{\boldsymbol{\theta}}_i, j, k) - \mu_Q^{new}(j,k)}{\sigma_Q^{new}(j,k)}\right]^2 \quad (7)$$

where P_e, Q_e and N have the same meaning as in Eqs. (2, 3). F_P and F_P^{new} (resp. F_Q and F_Q^{new}) have the same analytical expression; the former involves the averages and standard deviations collected in the training phase, while the averages and standard deviations collected at the new operating point are used in the latter;
5) the scores (6, 7) are used to assess the accuracy of the available equivalents in the new operating conditions. This consists of comparing, for each disturbance, the score obtained with the parameters $\hat{\boldsymbol{\theta}}_i$ of the i-th equivalent $(i = 1, ..., E)$ with the worst score obtained in the training phase when identifying $\hat{\boldsymbol{\theta}}_i$. If one or several available equivalents pass the accuracy test, there is no need to identify a new one; the equivalent showing the highest accuracy is selected. Otherwise a new equivalent has to be added to the existing set, i.e. a new $\hat{\boldsymbol{\theta}}_i$ has to be determined.

The computational burden can be shared between the TSO and the DSO. If confidentiality of the ADN data is an issue, Steps 1, 2 and 3 have to be taken care by the DSO.

B. Building a new equivalent with minimal update effort

When identifying an equivalent for new operating conditions, it can be expected that the values of some parameters, inherited from former equivalents, change very little, so that a complete new identification could be avoided. To identify the parameters of concern, a procedure inspired of the LASSO method can be used. That method was proposed in [28] for linear regression.

Once the accuracy of each parameter vector $\hat{\boldsymbol{\theta}}_i$ has been assessed on the d disturbances, the best among them is used as reference for the new operating conditions. It is defined as:

$$\hat{\boldsymbol{\theta}}^{ref} = \arg\min_{i=1,\ldots,E} \frac{1}{d}\sum_{j=1}^{d}\left[F_P^{new}(\hat{\boldsymbol{\theta}}_i, j) + F_Q^{new}(\hat{\boldsymbol{\theta}}_i, j)\right] \quad (8)$$

The goal is to minimize the number of parameters to adjust. To that purpose, the following minimization is considered:

$$\min_{\boldsymbol{\theta}} \quad F(\boldsymbol{\theta}) + \lambda \sum_{l=1}^{n} |\hat{\theta}_l^{ref} - \theta_l| \tag{9}$$

$$\text{subject to} \quad (1-\alpha)\,\hat{\boldsymbol{\theta}}^{ref} \leq \boldsymbol{\theta} \leq (1+\alpha)\,\hat{\boldsymbol{\theta}}^{ref} \tag{10}$$

where $0 \leq \alpha \leq 1$ controls the space searched around $\hat{\boldsymbol{\theta}}^{ref}$, n is the number of parameters in $\boldsymbol{\theta}$ and $F(\boldsymbol{\theta})$ decomposes into:

$$F(\boldsymbol{\theta}) = \frac{1}{c} \sum_{j=1}^{c} \left[F_P^{new}(\boldsymbol{\theta}, j) + F_Q^{new}(\boldsymbol{\theta}, j) \right] \tag{11}$$

The second term in (9) is a penalty, controlled by the scaling factor λ. It tends to make θ_l depart from θ_l^{ref} only if this yields a significant decrease of $F(\boldsymbol{\theta})$, i.e. if θ_l has a significant influence on $F(\boldsymbol{\theta})$. To save computing time, only the c disturbances ($c \leq d$) with the worst scores (i.e. highest values) $F_P(\hat{\boldsymbol{\theta}}^{ref}, j)$ and $F_Q(\hat{\boldsymbol{\theta}}^{ref}, j)$ are processed.

The value of α is chosen to keep $\boldsymbol{\theta}$ in realistic ranges of values. A typical value for α is 0.5, possibly increased if some parameters hit their bounds and an acceptable value of $F(\boldsymbol{\theta})$ has not been reached yet.

Simulation results have shown that $F(\hat{\boldsymbol{\theta}}_{ref})$ is a good choice of initial value for λ. The procedure thus starts with $\lambda = F(\hat{\boldsymbol{\theta}}_{ref})$. After a few iterations of the DE algorithm, if no significant improvement of $F(\boldsymbol{\theta})$ is obtained, λ is decreased and the minimization problem (9)-(11) is solved again. Decreasing λ yields smaller values of $F(\boldsymbol{\theta})$. The steps are repeated until the accuracy condition (5) is satisfied for the c disturbances. At this point, the components of $\hat{\boldsymbol{\theta}}$ and $\boldsymbol{\theta}^{ref}$ are compared. For the l-th component ($l = 1, \ldots, n$), if:

$$\frac{|\hat{\theta}_l - \theta_l^{ref}|}{\theta_l^{ref}} \leq \delta \tag{12}$$

the parameter of concern is considered to have little impact, since constraining θ_l to remain close to its reference θ_l^{ref} has little impact on the final scores $F_P(\hat{\boldsymbol{\theta}}, j)$ and $F_Q(\hat{\boldsymbol{\theta}}, j)$. While the DE algorithm updates all parameters simultaneoulsy, the "non-significant" parameters are left to their current values and are not considered in the subsequent identification steps. The criterion (5) is then checked for the remaining $d - c$ disturbances. If it fails, the disturbance with the worst simulated response is added ($c := c + 1$) and the objective function (11) is minimized by adjusting the reduced set of parameters. This is repeated until (5) is satisfied for all d disturbances.

C. Simulation results

Simulation results are reported on the test system of Section III-E, shown with its equivalent in Fig. 5.

Four different operating conditions are considered involving different load consumptions, wind speeds and irradiation levels, as shown in Table I. They have been selected from a larger set of 12 operating conditions detailed in [17]. OP1 is the operating point considered in Section III-E.

Assume that, initially, a single equivalent is available (i.e. $E = 1$), which was determined at OP1 and has the vector of parameters $\hat{\boldsymbol{\theta}}_1$.

TABLE I
OPERATING POINTS AND ASSOCIATED EQUIVALENT PARAMETERS $\hat{\boldsymbol{\theta}}_i$

	load	PV generation	wind generation	$\hat{\boldsymbol{\theta}}_i$
OP1	19.8 MW 10 % motors	mild irradiation 3.4 MW	strong wind 6.4 MW	$\hat{\boldsymbol{\theta}}_1$
OP2	19.8 MW 10 % motors	mild irradiation 3.4 MW	weak wind 1.6 MW	$\hat{\boldsymbol{\theta}}_1$
OP3	14.9 MW 60 % motors	no irradiation 0.0 MW	strong wind 6.4 MW	$\hat{\boldsymbol{\theta}}_2$
OP4	16.8 MW 10 % motors	mild irradiation 2.7 MW	strong wind 6.4 MW	$\hat{\boldsymbol{\theta}}_3$

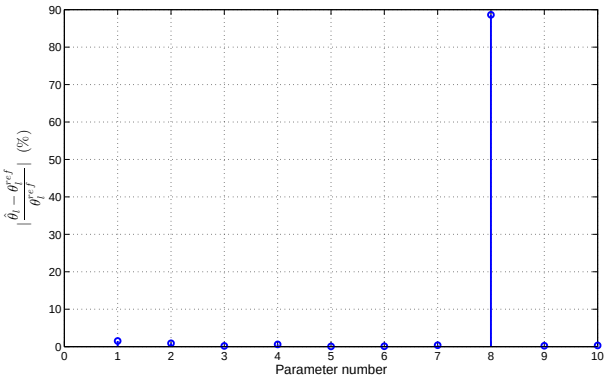

Fig. 10. OP3 : final values of $|\hat{\theta}_l - \theta_l^{ref}|/\theta_l^{ref}$ (in %), with $\boldsymbol{\theta}^{ref} = \hat{\boldsymbol{\theta}}_1$. The first 10 components are considered; the others are treated separately [16]

Consider that the ADN operates at OP2, which differs from OP1 by a lower wind input. The scores (6, 7) are computed for each of the $d = 14$ disturbances. The accuracy test of Step 5 is performed using $\hat{\boldsymbol{\theta}}_1$. The test is passed for all disturbances. Therefore, no new identification is required and $\hat{\boldsymbol{\theta}}_1$ can be used for both OP1 and OP2. In fact, updating the initial active and reactive powers of the equivalent IBG (namely P_2 and Q_2 in Fig. 5) turns out to be sufficient for accuracy. The same holds true for the equivalent load.

Consider now that the ADN operates at OP3. This is a nighttime scenario, with no PV irradiation and a smaller load power compared to OP1 and OP2. A higher proportion of induction motor load is also assumed (to account for a larger fraction of non-residential loads, for instance). The accuracy test of Step 5 is performed using $\hat{\boldsymbol{\theta}}_1$ (the only equivalent parameters available so far) and reveals two disturbances with low accuracy. These disturbances are used to identify the parameters with significant impact, using the procedure presented in Section IV-B.

Figure 10 shows the parameter relative variations defined in (12), with $\boldsymbol{\theta}^{ref} = \hat{\boldsymbol{\theta}}_1$. It shows very clearly that among the 10 components of $\boldsymbol{\theta}$, only the 8th one has impact on the accuracy of the equivalent. This parameter is $(\frac{di_p}{dt})_{max}$, the maximum rate of active current recovery of the equivalent IBG. Thus, $\hat{\boldsymbol{\theta}}_1$ is updated into $\hat{\boldsymbol{\theta}}_2$. With $\hat{\boldsymbol{\theta}}_2$ used in the equivalent, the targeted accuracy is achieved for all 14 disturbances and no further processing is required.

As a confirmation, Fig. 11 shows the active power P_e of the equivalent in response to a severe voltage dip, using $\hat{\boldsymbol{\theta}}_1$ and $\hat{\boldsymbol{\theta}}_2$,

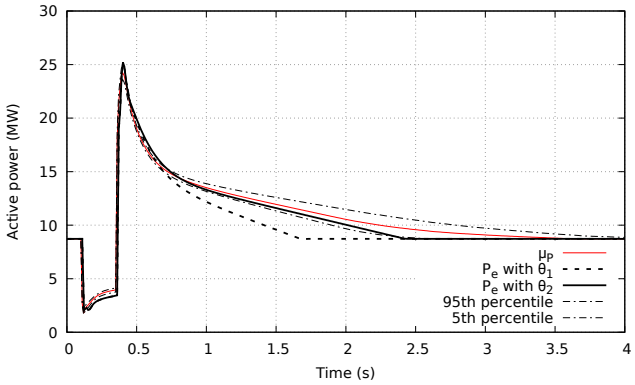

Fig. 11. OP3 : active power response of the equivalent to a severe voltage dip, using $\hat{\boldsymbol{\theta}}_1$ and $\hat{\boldsymbol{\theta}}_2$, respectively

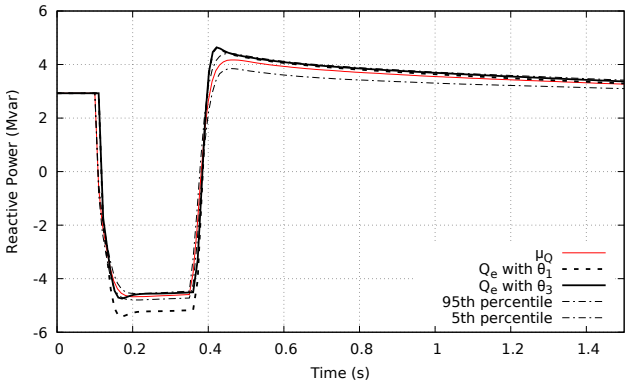

Fig. 13. OP4 : reactive power response of the equivalent to a severe voltage dip, using $\hat{\boldsymbol{\theta}}_1$ and $\hat{\boldsymbol{\theta}}_3$, respectively

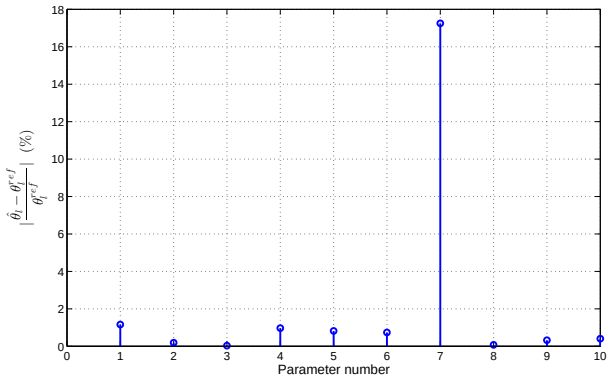

Fig. 12. OP4 : final values of $|\hat{\theta}_l - \theta_l^{ref}|/\theta_l^{ref}$ (in %) with $\boldsymbol{\theta}^{ref} = \hat{\boldsymbol{\theta}}_1$. The first 10 components are considered; the others are treated separately [16]

respectively. They are compared with the average active power response μ_P obtained from MC simulations. It can be seen that the response of the equivalent involving $\hat{\boldsymbol{\theta}}_1$ is not satisfactory because $(\frac{di_p}{dt})_{max}$ is set too high (allowing too fast a power recovery of the IBG). After adjusting this parameter in $\hat{\boldsymbol{\theta}}_2$, the figure confirms a much better match between P_e and μ_P.

It makes sense that $(\frac{di_p}{dt})_{max}$ is affected by the change of operating conditions. Indeed, since the PV units do not produce, less active power is sacrificed in favour of reactive current injection, and the average rate of recovery of the IBGs decreases. It is appealing that the results of the automatic LASSO-based procedure matches "engineering judgment".

Consider finally operation of the ADN at OP4. This scenario is identical to OP1 except that one feeder is out of service, as shown by the red cross in Fig. 5. This results in a decrease of 3 MW of load, 1.4 MW of PV capacity and 0.7 MW of PV production.

The accuracy test shows that neither $\hat{\boldsymbol{\theta}}_1$ nor $\hat{\boldsymbol{\theta}}_2$ suits all c disturbances. However, $\hat{\boldsymbol{\theta}}_1$ shows better results than $\hat{\boldsymbol{\theta}}_2$. The approach of Section IV-B is thus applied with $\hat{\boldsymbol{\theta}}_{ref} = \hat{\boldsymbol{\theta}}_1$.

The resulting variations of $\boldsymbol{\theta}$ with respect to $\hat{\boldsymbol{\theta}}_1$ is shown in Fig. 12. It shows that only the 7th component has an impact and should be adjusted. This parameter is the nominal current I_{nom} of the equivalent IBG. Thus, $\hat{\boldsymbol{\theta}}_1$ is updated into $\hat{\boldsymbol{\theta}}_3$. With $\hat{\boldsymbol{\theta}}_3$ used in the equivalent, the desired accuracy is obtained for all d disturbances and no further processing is required.

The improvement brought by this update can be seen in Fig. 13. The value of I_{nom} influences the reactive power response Q_e of the equivalent during the voltage dip essentially, when the IBGs are requested to inject reactive current to support their terminal voltage (see Fig. 3.b). With the adjusted value of I_{nom}, the reactive power Q_e rendered by the equivalent approaches more closely the average μ_Q obtained from MC simulations.

Furthermore it makes sense to adjust I_{nom} in the equivalent IBG, since a fraction of the total IBG capacity is out of service as a result of the feeder opening. Once again, the automatic LASSO-based method can be backed up by rather easy interpretations.

V. Validation of the Equivalent in a Long-Term Voltage Instability Scenario

A. Unreduced ADN and its equivalent

For the ADN part, the results reported in this section relate to a variant of the CIGRE MV Distribution Network Benchmark [20], whose one-line diagram is given in Fig. 14. The grid feeds residential as well as industrial loads. The dispersed IBGs fall in two categories : (i) large capacity (PV installations and a WT), and (ii) small residential (rooftop PVs). The former have fault-ride through and reactive current injection capabilities, the latter have not. The residential IBGs and loads have aggregated models connected behind an equivalent impedance accounting for Low Voltage (LV) transformers and feeders, as shown in the lower right corner of Fig. 14.

The initial power injections and flows are detailed in the same figure.

The topology of the equivalent is also shown in Fig. 14. The impedance $R_b + jX_b$ accounts for the MV grid, and $R_c + jX_c$ for the LV networks. The aggregated load and IBG attached to bus 1 account for residential loads and small-capacity IBGs. The parameters of this equivalent IBG are not included in $\boldsymbol{\theta}$ since it replaces small, residential LV installations that trip immediately for all considered disturbances (hence, its parameters have no influence on the dynamic response). As

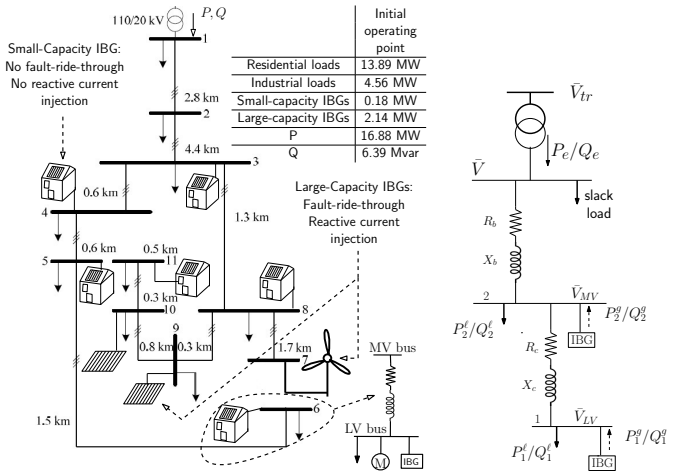

Fig. 14. Variant of the CIGRE MV Distribution Network Benchmark (left) and its dynamic equivalent (right)

regards the aggregated load and IBG at bus 2, they correspond to industrial loads and large-capacity IBGs, respectively.

B. Voltage instability scenario

The accuracy of the equivalent is checked in a long-term voltage instability scenario affecting the transmission system. Its response is compared to the response of the unreduced ADN, subject to the same transmission system weakening. Thus, instead of the sharp voltage changes considered in the training disturbances, the equivalent is checked against a slowly developing but pronounced voltage decay, typically caused by Load Tap Changers (LTCs) attempting to restore distribution voltages and overexcitation limiters protecting the synchronous machines [29].

As for the transmission part, the IEEE Nordic test system for voltage stability analysis and security assessment has been considered. This test system is fully documented in [30]. Its one-line diagram is reproduced in Fig. 15. The (insecure) operating point A has been considered. The initiating disturbance is a three-phase solid fault on line 4032-4044. The fault lasts 100 ms and is cleared by opening the line, which remains opened. Long-term voltage instability results.

The voltage evolutions shown in Fig. 16 relate to the transmission bus 1041, the most severely impacted, and the corresponding distribution bus 1, under LTC control. Until $t \simeq 70$ s, the LTC manages to keep the distribution voltage in its deadband, while subsequently it fails doing so, which is typical of voltage instability [29], [30].

Getting back to the ADN, the V_{tr} voltage on the high-voltage side of the transformer (see Fig. 14) is made to follow exactly the voltage at bus 1041 shown in Fig. 16. This is done in both MC simulations of the unreduced ADN model and in its equivalent. Note that the transformer is kept intact in the equivalent and its LTC is let to follow the distribution voltage variations as in the unreduced system model.

In a first step, the possible disconnection of IBGs due to low voltage is not taken into account. In Fig. 17 the evolution of the active power obtained from the equivalent is compared

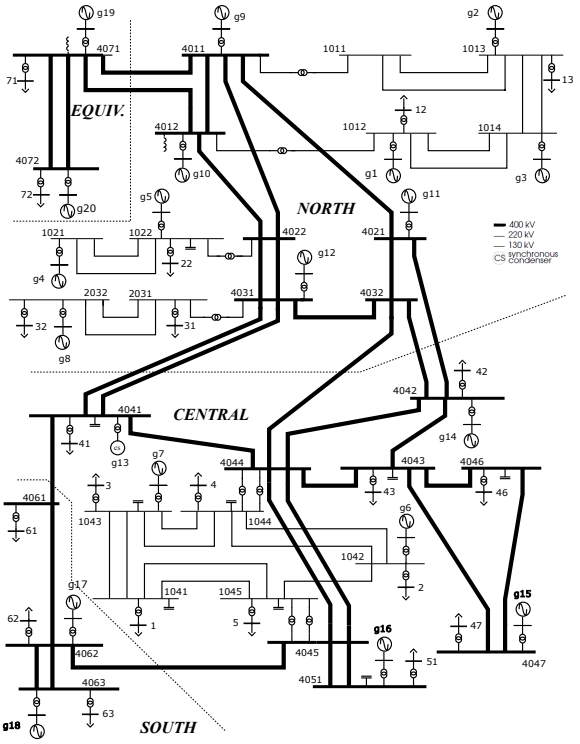

Fig. 15. IEEE Nordic test system [30]

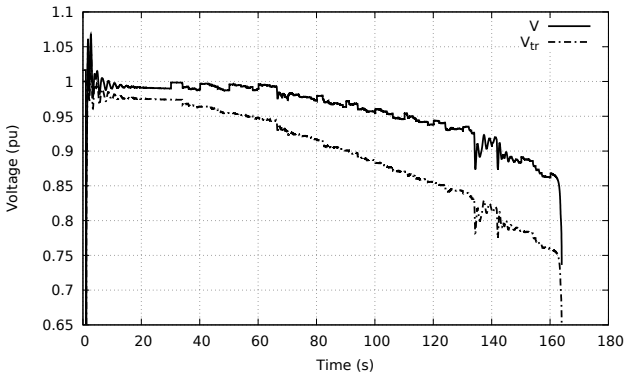

Fig. 16. IEEE Nordic test system : transmission and distribution voltages

to the average evolution μ_P. Similar results for the reactive power are given in Fig. 18. For clarity, the figures focus on the time interval that follows the line opening. The equivalent accurately reproduces the response of the unreduced system, in spite of a small shift of the reactive power response. Expectedly, the more depressed the transmission voltage, the more pronounced the discrepancy. The first tap change takes place at $t = 30$ s and subsequently every 10 s. Its effect is seen in the reactive power spikes.

In a second step, the disconnection of IBGs is considered. Figure 19 shows the corresponding active power evolutions. Starting from some time, the response of the equivalent is delayed with respect to the average response of the unreduced ADN. Indeed, the disconnection of the large-capacity IBGs in the unreduced system takes place around $t = 135$ s, while the aggregate IBG in the equivalent trips around $t = 145$ s.

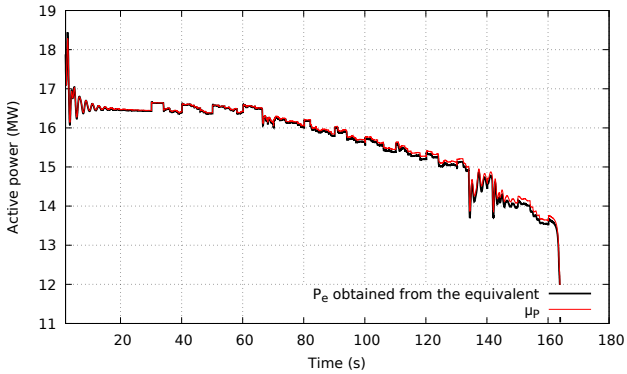

Fig. 17. Active power flow into the ADN and its equivalent. Disconnection of IBGs not modelled

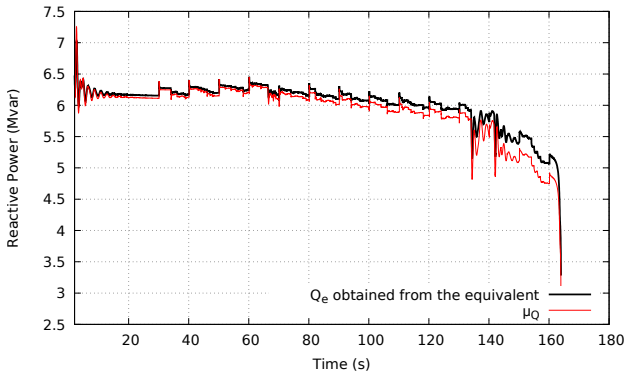

Fig. 18. Reactive power flow into the ADN and its equivalent. Disconnection of IBGs not modelled

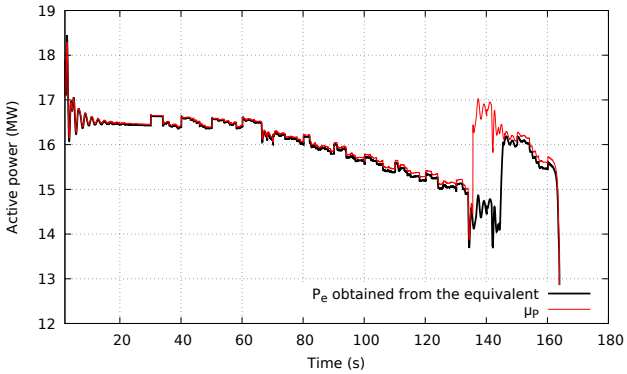

Fig. 19. Active power flow into the ADN and its equivalent. Disconnection of IBGs taken into account

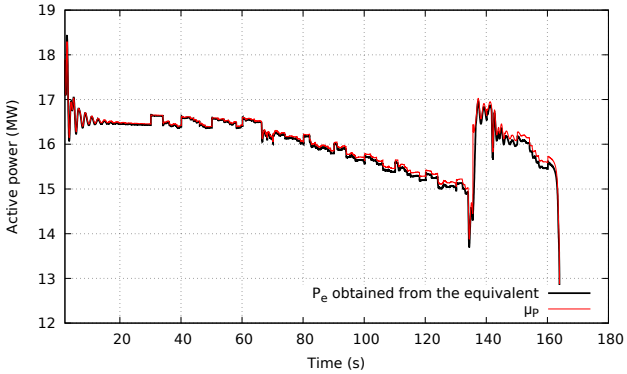

Fig. 20. Active power flow into the ADN and its equivalent. Disconnection of IBGs taken into account and LVRT curve of the equivalent IBG adjusted

This is caused by the lumping approximation in the equivalent, which results in a difference between the terminal voltage of the aggregate IBG and the voltages of the individual IBGs dispersed in the network. In most studies, that shift in time is inconsequential, since the system is clearly unstable with a transmission voltage around 0.8 pu at $t = 135$ s (see Fig. 16). Nevertheless, the discrepancy can be eliminated as follows.

With reference to the LVRT characteristic in Fig. 3.a, the IBG disconnects when the progressively sagging voltage crosses the V_r threshold and stays below for a duration $T_2(= 1.5$ s). Now, when training the equivalent with voltage dips the voltage either recovered above V_r or crossed the LVRT curve earlier. Hence, the V_r parameter was not "learnt" from the training disturbances but set the standard value of 0.90 pu. A small adjustment of V_r in the equivalent makes the IBG trip at the same time as the original IBGs. This is illustrated in Fig. 20 where V_r has been increased from 0.90 to 0.92 pu.

Note that all the other components of $\boldsymbol{\theta}$ were correctly identified from voltage dip disturbances. The same equivalent can be used in both short- and long-term voltage studies, as will be illustrated in the next section.

VI. Use Case of the Equivalent in Short- and Long-Term Voltage Stability Study

This section illustrates the use of the ADN equivalent in voltage stability studies, and its ability to reproduce the effects on transmission voltages of IBGs at distribution level.

A. Test system

The test system has been set up as follows.

For the transmission part, the IEEE Nordic test system presented in Section V-B has been reused, except for the distribution transformers in the Central region (see Fig. 15), which have been replaced as explained next.

The Central region is supposed to feed ADNs with a rather large penetration of renewable energy sources. This has been modelled by connecting to each transmission bus of the Central region a number of ADN equivalents in parallel, in replacement of the existing distribution transformer, as sketched in Fig. 21. The Central region has been selected as it is the most affected by voltage instability [30]. Outside the Central region the original distribution transformers and loads have been left unchanged.

The ADN used as reference is the 75-bus system already considered in Section III-E and shown in Fig. 5 together with its equivalent, derived as explained in Section III.

To reflect the diversity of the distribution grids that they replace, the various ADN equivalents have been randomized. The parameters varied from one instance of the equivalent to another are listed in Table II, together with their ranges of variation.

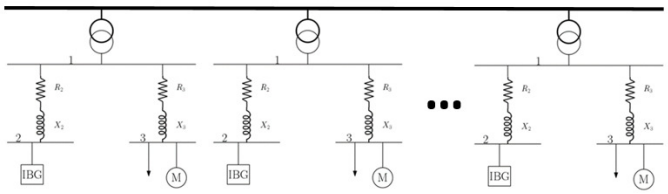

Fig. 21. Connection of multiple ADN equivalents to a transmission bus (in the Central region of the IEEE Nordic test system)

TABLE II
RANDOMIZED PARAMETERS OF THE ADN EQUIVALENTS

Static part of aggregate load	exponent α in Fig. 2	[1.35 1.83]
	exponent β in Fig. 2	[1.92 2.60]
Motor part of aggregate load	loading factor	[0.48 0.64]
	fraction m of initial power	[0.1 0.3]
Aggregate IBG	nominal apparent power S_{ibg} ("small" and "large" capacity) (MVA)	[5 10] [10 15]
	maximum rate of active power recovery (pu/s)	[0.3 0.4]
	slope k_{RCI} in Fig. 3.b	[2.93 3.96]
	fraction disconnected under low voltage	[0.10 0.15]
Impedances	R_1, X_1, R_2 and X_2	± 15 %
Distribution transformer	nominal apparent power S_{tfo} (MVA)	[18 22]
	delay before first tap change (s)	[28 32]
	time between further tap changes (s)	[8 12]

The IBG installed capacity can be compared to that of the distribution transformer through the *Capacity Ratio*:

$$CR = S_{ibg}/S_{tfo} \tag{13}$$

where S_{ibg} and S_{tfo} are defined in Table II. From the latter it is found that $CR \in [0.23\ 0.56]$ in the "small" IBG capacity scenario, and $CR \in [0.45\ 0.83]$ for the "large" capacity.

The power flows have been also varied inside the various equivalents. In particular the *Penetration Level* is defined as :

$$PL = P_2/(P_1 - P_2) \tag{14}$$

with P_1 and P_2 defined in Fig. 5. The average value over all instances is denoted $\overline{PL}$.

Note that the insertion of the ADN equivalents preserves the original operating point of the transmission system, which is point A in [30], as in Section V-B. The same holds true when $\overline{PL}$ is varied : for instance, a higher PL is obtained by increasing both the IBG production P_2 and the load P_1. All IBGs initially operate at unity power factor.

There is a total of 627 ADN equivalents substituted to the 11 loads of the Central area. The resulting model involves 68,527 differential/algebraic equations, which is only 3.7% of the number of similar equations if the ADNs were unreduced and connected to the transmission system. This would lead to a model with 47,088 buses vs. 1,944 when using equivalents.

B. Short-term dynamics

The same disturbance as in Section V-B is considered, i.e. a three-phase short-circuit on line 4032-4044, applied at $t = 1$ s and cleared in 100 ms by opening the line.

In this section, the focus is on short-term responses.

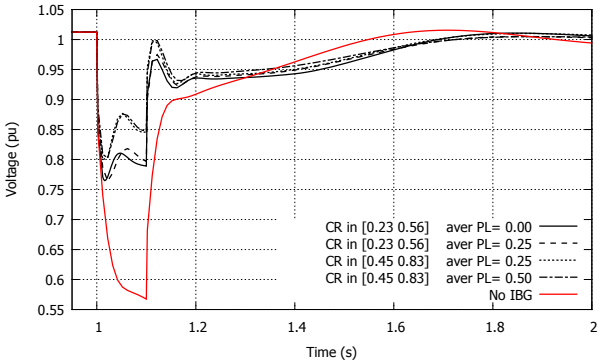

Fig. 22. IEEE Nordic test system with ADN equivalents. Voltage at bus 1041. Disconnection of IBGs not taken into account

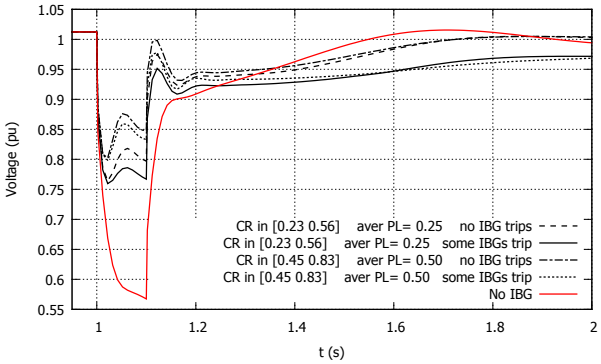

Fig. 23. IEEE Nordic test system with ADN equivalents. Voltage at bus 1041. Disconnection of IBGs taken into account

First, the IBG disconnection due to low voltage is not considered. Figure 22 shows the evolution of the voltage at the transmission bus 1041 for various combinations of CR and $\overline{PL}$. The curve labeled "No IBG" relates to the equivalent without IBG, while the curve $\overline{PL} = 0$ is provided for reference and relates to IBGs not producing but available for reactive current injection in low voltage conditions (see Section II-B2). The various curves show that:

- IBGs contribute to supporting the transmission voltage during the fault and shortly after its clearing;
- the larger CR, the stronger that support. Indeed, a larger CR value means a higher IBG capacity;
- the penetration level has almost no impact. Indeed, in response to falling transmission voltages, IBGs at distribution level give priority to reactive over active currents (see Section II-B3) and the pre-disturbance active powers do not really matter in such conditions.

Next, the disconnection of IBGs with voltages below the LVRT curve is taken into account, as mentioned in Section III-E, i.e. by reducing the power output of the IBG according to its terminal voltage, in each ADN equivalent separately. For two variants of CR and $\overline{PL}$ considered in Fig. 22, the voltage evolutions with and without disconnection can be compared in Fig. 23. IBG disconnection somewhat offsets the advantage of reactive current injection, since it increases the power drawn from the transmission grid.

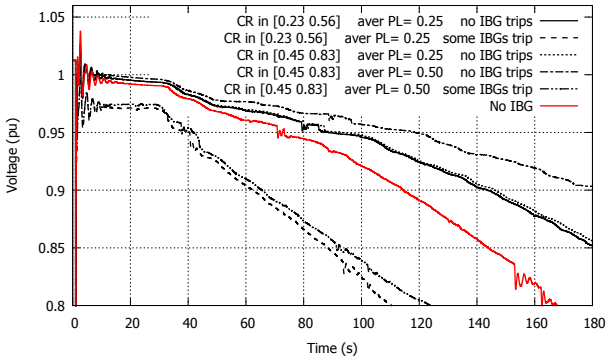

Fig. 24. IEEE Nordic test system with ADN equivalents. Voltage at bus 1041

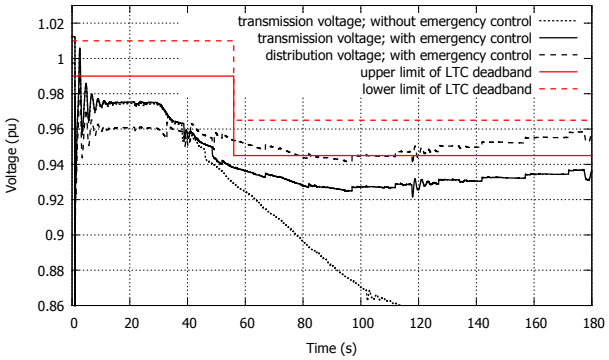

Fig. 25. IEEE Nordic test system with ADN equivalents. Voltages at bus 1041 and on the distribution side of a transformer connected to bus 1041

C. Long-term dynamics

The long-term evolution is now considered. Figure 24 shows the voltage evolution at bus 1041 during the three minutes that follow the line opening, for combinations of CR and $\overline{PL}$ values as well as with and without IBG disconnection.

Consider first the results with IBG disconnection disregarded. Comparing the upper four curves shows that IBGs do not prevent long-term voltage instability. For most of the simulated duration, IBGs behave as constant power sources. Indeed they start injecting reactive current when distribution voltages settle below $V_Q = 0.9$ pu (see Fig. 3.b), i.e. very lately. On the other hand, the LTCs tend to restore the distribution voltages to their setpoint and, hence, the load powers to their pre-disturbance values. Thus, the combined effects of IBGs and LTCs is a tentative restoration of the net power drawn from the transmission system to the same value as in case without IBGs, which is unstable.

While the final outcome is the same, IBGs slows down the fall of transmission voltage, which could give trained operators a bit more time to take remedial actions. The same three curves show that the higher $\overline{PL}$, the slower the voltage decay, while CR has no noticeable effect.

When IBG disconnection is accounted for, the opposite effect is noticed. A fraction of the IBG production is lost due to the short-circuit, and a 2.5 % lower voltage is already observed at $t = 20$ s. The loss of that local generation increases the net power drawn from the transmission system and accelerates voltage instability compared to the case without IBGs.

D. Long-term dynamics with corrective control

So far, only fast and local controls typically present in IBGs have been taken into account. In this last section, a slow and coordinated control of the IBGs connected to the same ADN is considered whose purpose is to counteract long-term voltage instability. The control scheme is detailed in [31] and can be summarized as follows.

The emergency control is triggered by an alarm stemming from the transmission grid. Quite a number of signals can be used to that purpose, ranging from simple voltage thresholds to voltage instability indicators [32]. At the moment the alarm is received, in each ADN, the voltage V_t on the transmission side of the main transformer is recorded into V_t^{min}, and the voltage V_d on the distribution side into V_d^{max}. The following actions are taken:

1) the LTC deadband is decreased to $[V_d^{max} - \epsilon \;\; V_d^{max} + \epsilon]$, where ϵ is the original half-deadband;
2) furthermore, if $V_d < V_d^{max} - \epsilon$, the LTC remains idle, i.e. the tap is not moved to increase V_d;
3) the reactive power of the IBGs are smoothly increased (provided they have reactive reserves and their terminal voltage is below the allowed limit).

The objective is to uplift V_t and keep it above V_t^{min}. Once this is achieved, actions 2 and 3 are disabled and the IBG reactive powers are blocked at their current values. If V_t falls again below V_t^{min}, actions 2 and 3 are re-activated.

In the equivalent, the reactive power ramp is applied to the aggregate IBG.

Figure 25 shows the stabilization of the voltage at bus 1041, in the scenario of Section VI-C with $CR \in [0.45\ 0.83]$ and $\overline{PL} = 0.50$. Corrective control is triggered by the transmission voltage V_t staying below 0.94 pu for more than three seconds (hence, $V_t^{min} = 0.94$ pu). This takes place at $t = 56$ s in the ADN of concern.

The same figure shows the voltage on the distribution side of a transformer connected to bus 1041, together with the LTC deadband. The latter is decreased at $t = 56$ s and the distribution voltage remains depressed, although at an acceptable value.

The reactive power of the equivalent IBG has been increased by 0.01 pu every 15 seconds until V_t settles above V_t^{min}. This rate has been chosen slow enough to let the LTC bring the distribution voltage within the decreased deadband and, hence, keep the load power decreased. Without that coordinated action on IBGs and LTCs, the distribution voltages and, hence, the load power would increase under the effect of the injected reactive power [31], and instability would not be avoided.

VII. Conclusion

It will be more and more important for TSOs to have accurate reduced-order models of the ADNs for incorporation into the dynamic simulations of their systems.

This paper has offered an overview and presented recent extensions of the authors' work on this issue. A number of desirable features have been stressed for the equivalent:

- account for the nonlinear behaviour of IBGs in response to large disturbances, in particular their possible disconnection in low voltage conditions;

- be applicable to realistic distribution system models;
- account for the uncertainty affecting dynamic models of the system to be reduced;
- be valid for a large variety of disturbances, while not overfitting one of them;
- keep the number of parameters to identify as small as possible, and discard those with little influence, for easier interpretation;
- be easily updated with changing operating conditions of the ADN;
- involve component models of the type typically used in time simulations.

The methodology presented in this paper allows obtaining the above features. Admittedly, the approach requires to set up the unreduced ADN model, and its implementation requires proper collaboration and coordination between the TSO and the DSOs, even more if ADN data confidentiality is a concern.

In terms of simulation results:

- the accuracy of the equivalent has been shown in a realistic long-term voltage instability scenario, quite different from the voltage dips used for training the equivalent;
- a use case has been detailed, involving numerous instances of the equivalent. This was an opportunity to illustrate the impact of IBG controls on short- and long-term voltage (in)stability.

Finally, the following extensions are considered:

- accounting for the stalling and tripping of induction motors, by extending the procedure used for IBGs;
- although it is not bound to a particular model, checking the approach with other type of loads, such as residential single-phase induction motors.

REFERENCES

[1] Ren 21, "Renewables 2019 Global Status Report," 2019.

[2] N. Hatziargyriou (convenor), "Contribution to Bulk System Control and Stability by Distributed Energy Resources connected at Distribution Network," *IEEE PES Tech. Report PES-TR22*, 2017.

[3] M. G. Dozein, P. Mancarella, T. K. Saha and R. Yan, "System strength and weak grids: fundamentals, challenges, and mitigation strategies," *2018 Australasian Universities Power Engineering Conference(AUPEC)*, 2018.

[4] K. W. Jones et al., "Impact of inverter based generation on bulk power system dynamics and short-circuit performance," Report of IEEE PES Task Force on Short-Circuit and System Performance Impact of Inverter Based Generation, IEEE PES Tech. Rep. PES-TR68, 2018.

[5] P. Aristidou and T. Van Cutsem, "A Parallel Processing Approach to Dynamic Simulations of Combined Transmission and Distribution Systems," *International Journal of Electrical Power & Energy Systems*, vol. 72, pp. 58–65, 2015.

[6] R. Venkatraman, S. K. Khaitan and V. Ajjarapu, "Dynamic co-simulation methods for combined transmission-distribution system with integration time step impact on convergence", *IEEE Transactions on Power Systems*, vol. 34, no. 2, pp. 1171–1181, 2018.

[7] A. Bharati and V. Ajjarapu, "Investigation of relevant distribution system representation with DG for voltage stability margin assessment", *IEEE Transactions on Power Systems*, vol. 35, no. 3, pp. 2072–2081, 2019.

[8] North American Electric Reliability Corporation (NERC), "Distributed Energy Resources Connection Modeling and Reliability Considerations," February, 2017.

[9] F. Conte, F. D'Agostino, S. Massucco, G. Palombo, F. Silvestro, C. Bossi and M. Cabiati, "Dynamic equivalent modelling of active distribution networks for TSO-DSO interactions," *Innovative Smart Grid Technologies Conference Europe (ISGT-Europe), 2017 IEEE PES*, Torino (Italy), 2017.

[10] J. V. Milanovic et al., "Modelling and aggregation of loads in flexible power networks", *Report of CIGRE Working Group C4.605*, 2014.

[11] G. Chaspierre, P. Panciatici and T. Van Cutsem, "Aggregated Dynamic Equivalent of a Distribution System hosting Inverter-based Generators," *Proc. 20th PSCC conference*, Dublin (Ireland), 2018.

[12] X. Wu, X. Lei, Y. Lan, A. Monti and F. Gao, "A New Dynamic Equivalent of Active Distribution Network for Transient Analysis," *2018 International Conference on Power System Technology (POWERCON)*, pp. 529–539, Guangzhou (China), 2018.

[13] F. Conte, F. D'Agostino and F. Silvestro, "Operational constrained nonlinear modeling and identification of active distribution networks," *Electric Power Systems Research*, vol. 168, pp. 92-104, 2019.

[14] X. Shang, Z. Li, J. Zheng and Q.H. Wu, "Equivalent modeling of active distribution network considering the spatial uncertainty of renewable energy resources," *International Journal of Electrical Power and Energy Systems*, vol. 112, pp. 83-91, 2019.

[15] N. Fulgêncioa, C. Moreira, L. Carvalho and J. P. Lopes, "Aggregated dynamic model of active distribution networks for large voltage disturbances," *Electric Power Systems Research*, vol. 178, pp. 1–13, 2019.

[16] G. Chaspierre, G. Denis, P. Panciatici and T. Van Cutsem, "An Active Distribution Network Equivalent Derived From Large-Disturbance Simulations With Uncertainty," *IEEE Transactions on Smart Grid*, vol. 11, no. 6, pp. 4749– 4759, November 2020.

[17] G. Chaspierre, *Reduced-order modelling of active distribution networks for large-disturbance simulations*, PhD Thesis, University of Liège (Belgium), Oct. 2020, available at https://orbi.uliege.be/handle/2268/251602

[18] A. Radovanovic, J. V. Milanovic, "Exploratory Study Towards Dynamic Equivalent Modelling of Hybrid Renewable Energy Source Plant Based on Historical Production Data," *IEEE Milan PowerTech conference*, 2019.

[19] E. O. Kontis, T. A. Papadopoulos, M . H. Syed, E. Guillo-Sansano, G. M. Burt, G. K. Papagiannis, "Artificial-Intelligence Method for the Derivation of Generic Aggregated Dynamic Equivalent Models," *IEEE Transactions on Smart Grid*, vol. 34, No. 4, pp 2947-2956, 2019.

[20] S. Barsali et al. "Benchmark systems for network integration of renewable and distributed energy resources", Report of CIGRE Task Force C6.04, 2014.

[21] P. Kundur, *Power system stability and control,* McGraw-hill New York, 1994.

[22] IEEE Standards Coordinating Committee 21, "IEEE Standard for Interconnection and Interoperability of Distributed Energy Resources with Associated Electric Power Systems Interfaces," Approved 15 February, 2018.

[23] "Commission Regulation (EU) 2016/631 of 14 April 2016 establishing a network code on requirements for grid connection of generators," pp. 1-68, 27 April 2016. Available: https://www.entsoe.eu/network_codes/rfg/. [Accessed October 2019].

[24] K.V. Price, R.M. Storn and J.A. Lampinen, *Differential Evolution - A Practical Approach to Global Optimization,* Springer, Heidelberg (Germany), 2005.

[25] L. Ljung, *System identification: theory for the user.* PTR Prentice Hall, Upper Saddle River, NJ, 1999.

[26] F. Bu, Z. Ma, Y. Yuan and Z. Wang, "WECC Composite Load Model Parameter Identification Using Evolutionary Deep Reinforcement Learning," *IEEE Transactions on Smart Grid*, vol. 11, no. 6, pp. 5407 - 5417, 2020.

[27] P. Aristidou, D. Fabozzi and T. Van Cutsem, "Dynamic simulation of large-scale power systems using a parallel Schur-complement-based decomposition method," *IEEE Trans. on Parallel and Distributed Systems,* vol. 25, no. 10, pp. 2561-2570, 2014.

[28] R. Tibshirani,"Regression shrinkage and selection via the LASSO," *Journal of the Royal Statistical Society. Series B*, vol. 58, no. 1, pp. 267-288, 1996.

[29] T. Van Cutsem and C. Vournas., *Voltage Stability of Electric Power Systems*, Springer (previously Kluwer Academic Publishers), Norwell, NJ, 1998. ISBN 978-0-7923-8139-6.

[30] T. Van Cutsem et al., "Test Systems for Voltage Stability Analysis and Security Assessment," Report of IEEE PES Task Force on Test Systems for Voltage Stability and Security Assessment, IEEE PES Tech. Rep. PES-TR19, 2015.

[31] L. D. Pabon Ospina and T. Van Cutsem, "Emergency support of transmission voltages by active distribution networks: a non-intrusive scheme," *IEEE Transactions on Power Systems (in press)*, 2020.

[32] M. Glavic and T. Van Cutsem, "A short survey of methods for voltage instability detection", Proc. 2011 IEEE PES General Meeting, pp. 1-8